



HAL
open science

Suspected seismo-ionospheric coupling observed by satellite measurements and GPS TEC related to the M7.9 Wenchuan earthquake of 12 May 2008

K Ryu, Michel Parrot, S.G. Kim, K.S. Jeon, S Pulnits, K.-I Oyama

► **To cite this version:**

K Ryu, Michel Parrot, S.G. Kim, K.S. Jeon, S Pulnits, et al.. Suspected seismo-ionospheric coupling observed by satellite measurements and GPS TEC related to the M7.9 Wenchuan earthquake of 12 May 2008. *Journal of Geophysical Research Space Physics*, 2014, 119, pp.10305-10323. 10.1002/2014JA020613 . insu-01172657

HAL Id: insu-01172657

<https://insu.hal.science/insu-01172657>

Submitted on 7 Jul 2015

HAL is a multi-disciplinary open access archive for the deposit and dissemination of scientific research documents, whether they are published or not. The documents may come from teaching and research institutions in France or abroad, or from public or private research centers.

L'archive ouverte pluridisciplinaire **HAL**, est destinée au dépôt et à la diffusion de documents scientifiques de niveau recherche, publiés ou non, émanant des établissements d'enseignement et de recherche français ou étrangers, des laboratoires publics ou privés.

RESEARCH ARTICLE

10.1002/2014JA020613

Key Points:

- Ionospheric disturbances before the Wenchuan earthquake are analyzed
- The TEC increase is revealed as the gradual EIA enhancements
- The nighttime data provide clues about geometry of seismo-ionospheric coupling

Correspondence to:

K. Ryu,
kwangsun@kaist.ac.kr

Citation:

Ryu, K., M. Parrot, S. G. Kim, K. S. Jeong, J. S. Chae, S. Pulnits, and K.-I. Oyama (2014), Suspected seismo-ionospheric coupling observed by satellite measurements and GPS TEC related to the M7.9 Wenchuan earthquake of 12 May 2008, *J. Geophys. Res. Space Physics*, 119, 10,305–10,323, doi:10.1002/2014JA020613.

Received 15 SEP 2014

Accepted 11 NOV 2014

Accepted article online 15 NOV 2014

Published online 5 DEC 2014

Suspected seismo-ionospheric coupling observed by satellite measurements and GPS TEC related to the M7.9 Wenchuan earthquake of 12 May 2008

K. Ryu¹, M. Parrot², S. G. Kim¹, K. S. Jeong¹, J. S. Chae¹, S. Pulnits³, and K.-I. Oyama⁴

¹Satellite Technology Research Center, KAIST, Daejeon, South Korea, ²LPC2E/CNRS 3A, Avenue de la Recherche Scientifique, Orléans, France, ³Space Research Institute, Russian Academy of Sciences, Moscow, Russia, ⁴Center for Space Weather Study and Education, Kyushu University, Hakozaki, Fukuoka, Japan

Abstract Anomalous changes in the ionospheric conditions related to the Wenchuan earthquake of 12 May 2008 are investigated using electron density (N_e) from Detection of Electro-Magnetic Emissions Transmitted from Earthquake Regions (DEMETER) and CHAMP satellites, electric field from DEMETER, and GPS-total electron content (TEC) maps. The normalized N_e from the DEMETER satellite reveal that the previously reported TEC increments before the earthquake can be considered as fragments of the gradual equatorial ionization anomaly (EIA) enhancements near the epicenter longitude that began approximately 1 month before the earthquake and reached its maximum with an exceptionally large strength index 8 days prior to the main shock. This feature is indirectly confirmed through the CHAMP N_e and GPS TEC data. Following the EIA intensity peak, disturbances in the N_e and O^+ density were observed in the nightside. Based on the concurrent electric field and N_e changes, it is suggested that EIA intensification could be triggered by the E field disturbances over the epicenter.

1. Introduction

There have been numerous studies on observable precursors of earthquakes [Hayakawa *et al.*, 2000; Ondoh, 2003; Oyama *et al.*, 2008; Zhang *et al.*, 2011] and on the underlying mechanisms [Namgaladze *et al.*, 2009; Freund, 2010; Kuo *et al.*, 2011, 2014] that cause the ionospheric disturbances coupled to seismic activities. However, there has not yet been an indisputable and unified explanation for what triggers such anomalies and why they occur before and after seismic disturbances. Meanwhile, recent statistical analyses using ground [Fujiwara *et al.*, 2004; Liu *et al.*, 2006] and satellite [Li and Parrot, 2013] observations have provided persuasive correlations between the seismic activities and the ionospheric disturbances preceding earthquakes.

The previously investigated precursory phenomena of earthquakes are classified into several categories of plasma waves, plasma density (ionic and electronic) and temperature variations, energetic particles, infrared emissions, and so on. Larkina *et al.* [1989] reported an anomalous increase in the intensity of low-frequency (0.1–16 kHz) radio wave emissions detected in the INTERCOSMOS-19 satellite data when it was nearly over the epicenter of an earthquake zone. Theoretical studies have followed in order to explain the detected ELF/VLF emissions over the epicenter region [Gokhberg *et al.*, 1989; Sorokin and Chmyrev, 2002]. Boskova *et al.* [1993] reported significant changes in the light ions (H^+ and He^+) in the ion composition data from the low-altitude INTERCOSMOS-24 satellite. Chmyrev *et al.* [1997] analyzed the COSMOS-1809 satellite data for the ELF emissions, plasma density (N_e) and its variations (dN_e), in the ionosphere above the Spitak earthquake zone. Hayakawa *et al.* [2000] reported a correlation between the global distribution of seismic activity and ion density variations in the ionosphere, based on a large database of plasma densities measured by the INTERCOSMOS-24 satellite. Oyama *et al.* [2011] reported that the electron temperatures observed by the HINOTORI satellite around the epicenters of several large earthquakes that occurred in the Philippines in January 1982 significantly decreased in the afternoons several days before and after the earthquakes. Oyama *et al.* [2011] discovered ion density reductions in the ionosphere associated with a large earthquake ($M = 7.5$) observed by the US satellite DE-2. Furthermore, electric fields are said to be the most probable candidates for modifications of the ionosphere. Ryu *et al.* [2014a] reported the equatorial ionization anomaly (EIA) intensification before and after the M8.7 Sumatra earthquake of March 2005 and the M8.0 Pisco earthquake of August 2007 as observed by the CHAMP (CHALLENGING Mini-satellite Payload) and

DEMETER (Detection of Electro-Magnetic Emissions Transmitted from Earthquake Regions) satellites. They explained that changes in the ionospheric potential over the seismic region that accompany the converging zonal electric field can trigger upward (downward) plasma movement. Recently, *Ryu et al.* [2014b] extended the case studies to the statistical study using 6 year long DEMETER observation and revealed there exist significant cross correlation between the EIA intensity and the seismic activity in the regions with frequent earthquakes. *Aleksandrin et al.* [2003] analyzed the data of various near-Earth space experiments (MIR station, METEOR-3, GAMMA, and SAMPEX satellites) and reported that particle bursts were observed several hours before strong earthquakes. *Tronin* [1996] reported positive anomalies of the outgoing Earth radiation flux recorded at nighttime that were associated with the largest linear structures and fault systems of the crust.

Since the Wenchuan large earthquake in May 2008, a number of papers have been published that describe the precursory increase of the total electron content (TEC) related to the earthquake [*Zhao et al.*, 2008; *Pulinets et al.*, 2010; *Klimenko et al.*, 2011]. *Walker et al.* [2013] reported that an increase in ULF wave activity was found in the vicinity of the epicenter of the Wenchuan earthquake. Therefore, the ionospheric disturbances related to the Wenchuan earthquake of May 2008 have been revisited through investigating the N_e and O^+ densities, the electric field data of DEMETER [*Parrot*, 2002], and the N_e of CHAMP [*Lühr et al.*, 2012], in addition to the global VTEC data provided by the International GNSS (Global Navigation Satellite Systems) Service (IGS) [*Hernández-Pajares et al.*, 2009]. Based on these observations and the established theories, the mechanism of the seismo-ionospheric coupling in the midlatitude region is discussed in the context of the electromagnetic interactions of the ionospheric plasma.

2. Observations

2.1. Earthquake Occurrences and Space Weather Conditions

The M7.9 Wenchuan earthquake in China, also known as the Eastern Sichuan earthquake, occurred on 12 May 2008 (06:28 UTC) and struck the eastern edge of the Tibetan Plateau at 31.015°N, 103.365°E in the Longmenshan fault zone, which was formed as a result of the northward convergence of the India Plate against the Eurasia Plate with a velocity of 50 mm/yr.

Table 1 presents the global distribution of the large earthquakes ($M > 5.7$) that occurred during the study period (from D-40 to D+40). The main shock (36th in the list) and the spatially related large earthquakes are indicated using underlined numbers. As described in the list, the Wenchuan earthquake was characterized by the absence of foreshocks and high aftershock activity, which made forewarning of the devastating earthquake and averting damage practically impossible.

The spatial distribution of large earthquakes with $M > 5.0$ was depicted in Figure 1. As seen in the map, the Wenchuan earthquake and its aftershocks were the most dominant seismic activities during the study period and the seismic energy involved in the Wenchuan earthquake was at least 10 times larger than any of the other seismic events, considering the relationship between the magnitude of an earthquake (M_s , Richter magnitude) and the total radiated seismic energy (E_s , in joules), $\log E_s = 1.5M_s + 4.8$, established by *Gutenberg and Richter* [1956].

Figure 2 presents the solar wind conditions and geomagnetic activities for the study period (April to June 2008) around the occurrence of the earthquake. The same parameters for 2007 and 2008 are shown together for comparison. The solar wind conditions demonstrate that during this interval, the solar wind speed and density recurrently increased and decreased (Figures 2h and 2i). Furthermore, there were strong Alfvénic fluctuations in the interplanetary magnetic field (IMF) when the solar wind speed was high (Figures 2e–2g). For the solar wind and IMF, the OMNI data were used and time shifted to the Earth's bow shock nose from the location of the ACE spacecraft (for further details, refer to <http://omniweb.gsfc.nasa.gov>). These are features of the corotating interaction regions (CIRs). The geomagnetic activities caused by the high-speed solar wind streams with the strong Alfvénic fluctuations in the IMF are characterized by the continuous enhancement of the K_p or AE indexes, which are often referred to as high-intensity, long-duration, continuous AE activity [*Tsurutani and Gonzalez*, 1987].

Strong impacts of the high-speed solar wind streams on Earth's magnetosphere occurred on 23 April, approximately 19 days prior to the earthquake, and on 14 June, approximately 33 days after the earthquake. These resulted in moderate magnetic storms ($-30\text{nT} > Dst_{\min} > -60\text{nT}$) and increases of the K_p index greater than 3. Other impacts occurred evenly distributed in time, but they produced only moderate

Table 1. List of Large Earthquakes That Occurred Around the Wenchuan Earthquake (36th in the List)^a

No.	<i>M</i>	<i>D</i>	UT	Latitude	Longitude	Depth	Magnitude	No.	<i>M</i>	<i>D</i>	UT	Latitude	Longitude	Depth	Magnitude
1	4	7	22:54	-20.0	168.5	10.0	5.8	<u>36</u>	5	12	6:28	31.0	103.3	19.0	7.9
2	4	9	11:13	-20.2	168.9	16.0	6.4	<u>37</u>	5	12	6:43	31.2	103.7	10.0	5.8
3	4	9	11:23	-20.2	168.9	35.0	6.3	<u>38</u>	5	12	11:11	31.2	103.6	10.0	6.1
4	4	9	12:46	-20.1	168.9	33.0	7.3	<u>39</u>	5	13	7:07	30.9	103.2	9.0	5.8
5	4	9	14:47	-20.0	168.9	35.0	6.3	<u>40</u>	5	15	14:23	-57.9	-25.5	35.0	5.9
6	4	10	1:10	-20.3	168.9	35.0	5.8	<u>41</u>	5	17	17:08	32.2	105.0	9.0	5.8
7	4	11	16:35	-20.4	168.8	35.0	5.9	<u>42</u>	5	19	3:16	-47.8	32.0	10.0	5.9
8	4	11	17:45	-20.4	168.8	11.0	6.1	<u>43</u>	5	19	14:26	1.6	99.1	10.0	6.0
9	4	12	0:30	-55.7	158.5	16.0	7.1	<u>44</u>	5	20	13:53	51.2	178.8	27.0	6.3
10	4	14	9:45	-56.0	-28.0	140.2	6.0	<u>45</u>	5	23	19:35	7.3	-34.9	8.0	6.5
11	4	15	3:03	13.6	-90.6	33.0	6.1	<u>46</u>	5	24	13:24	-7.2	156.1	29.0	5.9
12	4	15	22:59	51.9	-179.4	11.0	6.4	<u>47</u>	5	24	19:20	4.3	-73.8	8.9	5.9
13	4	16	0:35	-18.6	-175.7	10.0	6.3	<u>48</u>	5	25	8:21	32.6	105.4	18.0	6.1
14	4	16	5:54	51.9	-179.2	13.0	6.6	<u>49</u>	5	25	19:18	56.1	-153.8	22.0	6.0
15	4	16	19:19	39.0	140.0	166.0	5.8	<u>50</u>	5	27	5:51	-56.6	147.4	10.0	5.9
16	4	18	20:39	-17.3	-179.0	553.8	6.3	<u>51</u>	5	29	15:46	64.0	-21.0	9.0	6.3
17	4	18	21:10	-27.5	-176.6	10.0	5.8	<u>52</u>	5	30	7:25	30.8	141.5	16.0	5.8
18	4	19	3:12	-7.8	125.7	13.0	6.1	<u>53</u>	5	31	4:37	-41.2	80.5	9.0	6.4
19	4	19	5:58	-20.3	168.8	14.0	6.3	<u>54</u>	5	31	23:16	-28.9	-112.3	10.0	5.8
20	4	19	10:21	-7.9	125.7	10.0	6.0	<u>55</u>	6	1	1:57	20.1	121.3	31.0	6.3
21	4	23	18:28	22.9	121.6	10.0	6.0	<u>56</u>	6	1	14:31	-59.4	149.7	10.0	6.5
22	4	24	12:14	-1.2	-23.5	10.0	6.5	<u>57</u>	6	3	16:20	-10.5	161.3	84.0	6.2
23	4	26	23:34	-49.1	164.1	10.0	6.1	<u>58</u>	6	3	17:31	-8.2	120.3	14.0	5.9
24	4	28	0:06	17.8	-100.2	56.9	5.8	<u>59</u>	6	3	21:03	-8.1	120.3	7.0	5.8
25	4	28	15:57	-58.7	-24.7	35.0	6.1	<u>60</u>	6	3	22:04	-8.1	120.2	14.0	6.0
26	4	28	18:33	-19.9	169.0	32.0	6.4	<u>61</u>	6	5	2:16	-38.8	-91.6	10.0	6.0
27	4	28	20:26	-20.2	168.8	35.0	6.1	<u>62</u>	6	5	5:22	-38.9	-91.6	7.0	5.8
28	4	29	5:26	41.5	142.0	46.7	5.8	<u>63</u>	6	6	13:42	-7.5	127.9	122.0	6.0
29	4	29	19:10	-6.1	127.5	404.7	5.9	<u>64</u>	6	8	12:25	38.0	21.5	16.0	6.4
30	5	2	1:33	51.9	-177.5	14.0	6.6	<u>65</u>	6	10	4:13	-18.1	167.9	35.0	5.9
31	5	3	19:01	-6.6	155.1	35.0	5.8	<u>66</u>	6	12	5:30	-50.2	-114.2	10.0	5.9
32	5	7	16:02	36.2	141.5	19.0	6.2	<u>67</u>	6	13	23:43	39.0	140.9	7.8	6.9
33	5	7	16:16	36.2	141.8	23.3	6.1	<u>68</u>	6	15	1:13	-17.7	-179.7	611.4	5.9
34	5	7	16:45	36.2	141.5	27.0	6.9	<u>69</u>	6	15	8:37	-36.6	-107.4	10.0	6.0
35	5	9	21:51	12.5	143.2	76.0	6.8	<u>70</u>	6	17	17:42	5.0	-82.7	10.0	5.9

^aThe earthquakes in the list have magnitudes greater than 5.7 and occurred globally between 40 days prior to and 40 days after the Wenchuan earthquake. Note that the underlined earthquake numbers represent the earthquakes that are spatially related to the Wenchuan earthquake.

disturbances in the *Kp* index. Near the earthquake occurrence, a moderate geomagnetic storm on 2 May occurred with a *Kp* of ~4.0. The solar wind conditions and geomagnetic activities data were used to determine if the observed disturbances resulted from a seismic origin or other effects.

The year 2008 was in the solar minimum phase right before the end of Solar Cycle 23. Thus, the $F_{10.7}$ solar flux level was very low, typically less than 80 solar flux unit, which indicates that the disturbances in the ionosphere that were directly caused by solar irradiance were insignificant. For the disturbances related to the seismo-ionospheric coupling process, the affected area would corotate with the Earth, and a disturbance would emerge when the longitudinal variations in the satellite measurements, at the same or a similar local time, were investigated. Weak solar activity and relatively quiet geomagnetic conditions around the

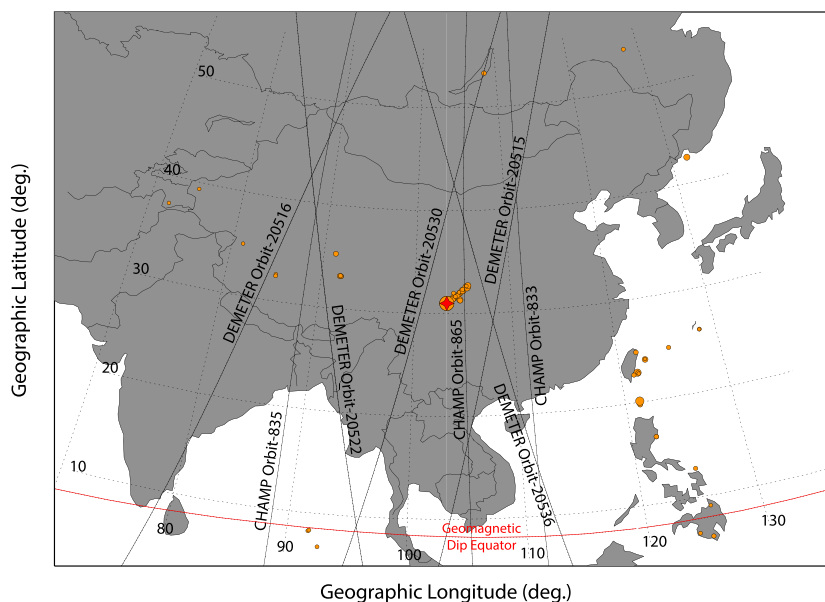


Figure 1. Geographic map illustrating the epicenter and the DEMETER and CHAMP satellite passes that are introduced explicitly in the text. The orbit numbers are indicated on the trajectories. The epicenter of the main earthquake is marked using a red star, while the epicenters of the large earthquakes that occurred during the study period (as listed in Table 1) are indicated by orange circles with diameters proportional to their magnitudes.

time of earthquake occurrence enabled the investigation and focus of the local variations of the ionosphere caused by seismic origins.

2.2. Observations and Data Processing

At the time of the earthquake, the polar orbiting satellites (DEMETER and CHAMP) were operational and provided observational data of the ionospheric F_2 region. DEMETER was launched on 29 June 2004 [Cussac *et al.*, 2006] to study the ionosphere disturbances caused by seismoelectromagnetic effects. DEMETER measured the ionospheric plasma parameters from a Sun-synchronous orbit, with a local equatorial crossing on an ascending node at 22:30. The orbit altitude was 710 km at the time of the launch and lowered to 660 km in December 2005, without changing the ascending node. The data measured by the retarding potential analyzer (Instrument d'Analyse du Plasma; IAP) [Berthelier *et al.*, 2006a], the electric field sensor (Instrument Champ Electrique; ICE) [Berthelier *et al.*, 2006b], and the Langmuir probe (Instrument Sonde de Langmuir; ISL) [Lebreton *et al.*, 2006] were used in this study. The instruments measured, in situ, the electron density, electron temperature, ion density, and ion temperature.

The German satellite CHAMP was launched in July 2000 into a circular, near-polar (inclination: 87°) orbit at 460 km altitude. During its lifetime, the orbit had slowly decayed to 350 km altitude by the end of 2007, with its final reentry into the atmosphere on 19 September 2010. The orbital plane processed through the local time at a rate of approximately 5.5 min per day, sweeping all time zones within 131 days. Among the various measurements, the electron density data collected by the PLP (Planar Langmuir Probe) were used in comparison with the other ionospheric measurements. The CHAMP electron density data were validated by McNamara *et al.* [2007].

For the complementary analyses, the IONospheric Map EXchange global ionospheric maps [Hernández-Pajares *et al.*, 2009] were used to verify whether the satellite measurements were consistent with the total electron content (TEC) values derived from the GPS. The global vertical TEC (VTEC) maps generated from worldwide-distributed GPS stations using the dual-frequency sounding method are distributed by the International GNSS (Global Navigation Satellite Systems) Service (IGS). In this study, the combined VTEC values, labeled as IGSG, with resolutions of 2 h, 5° , and 2.5° in time, longitude, and latitude, respectively, were used in combination with the in situ measurements.

For this study, the ionospheric measurement data from 2 April to 21 June (40 days prior to and after the earthquake on 12 May 2008: the 133rd day of the year) were collected and used in the analyses. For

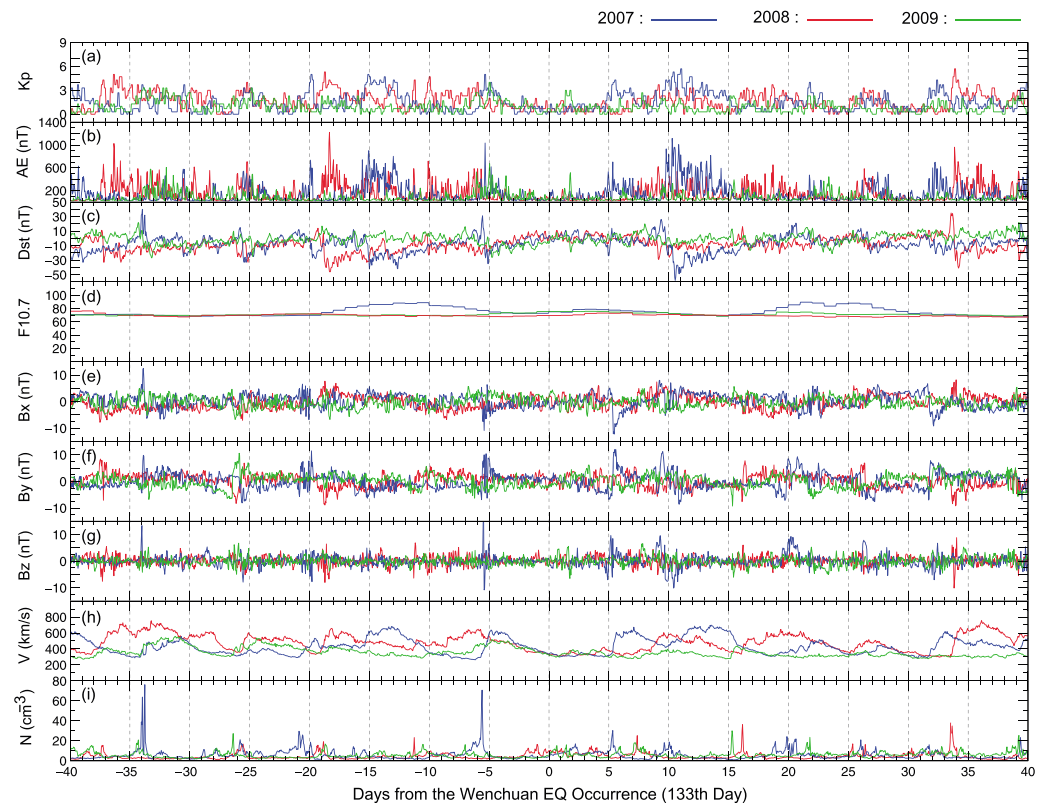


Figure 2. Geomagnetic indices, solar indices, and solar wind conditions around the main earthquake on 12 May 2008 (red). The same parameters for 2007 (blue) and 2009 (green) are shown for comparison. (a) *Kp* index, (b) *AE* index, (c) *Dst* index, (d) $F_{10.7}$ solar radio flux, interplanetary magnetic field (B_x : (e), B_y : (f), B_z : (g)), (h) solar wind speed, and (i) solar wind density.

comparison with the same season in other years, 80 days from 93rd day to 173rd day in 2007 and 2009 were also investigated in order to determine whether the observed anomaly around the earthquake was a seasonal variation. The DEMETER ionospheric data were obtained from the CDDP (Centre de Données de la Physique des Plasmas) operated by le Centre National d'Etudes Spatiales, and the CHAMP data via ISDC (Information System and Data Center) operated by the Helmholtz Centre Potsdam. The IGS global VTEC map was procured from CDDIS (Crustal Dynamics Data Information System) managed by NASA (National Aeronautics and Space Administration).

3. Results

3.1. DEMETER Observations of the EIA Enhancement

While investigating the DEMETER ionospheric data, it was realized that the electron density profile measured by the ISL in the dayside on D-8 (4 May) along Orbit-20515, whose longitudes in the trajectory passed very close to that of the epicenter, exhibited an anomalous increase in the equatorial region. The latitudinal profiles of all orbits during the 2 day period (from D-8 to D-7) are presented in Figure 3. Because DEMETER has a Sun-synchronous orbit, its orbit trajectories pass varying longitudes at a fixed local time (10:30 LT) in the dayside. This enabled the investigation of the regional anomalies regardless of the local time variations of the ionosphere. As shown in Figure 3a, the electron densities in the equator region along the orbits whose longitudinal distances were close to the epicenter are higher compared with the other orbits. The electron density profiles of the three orbits with longitudinal distances of less than 20° from the epicenter are presented in Figure 3b. Compared with the averaged electron density profile (the averaged values are the black solid line and the standard deviation ranges are the dashed lines in Figure 3), the three orbits (Orbit-20515 and Orbit-20516 on D-8 and Orbit-20530 on D-7) have apparently high electron density over the standard deviation range in the geomagnetic equator region.

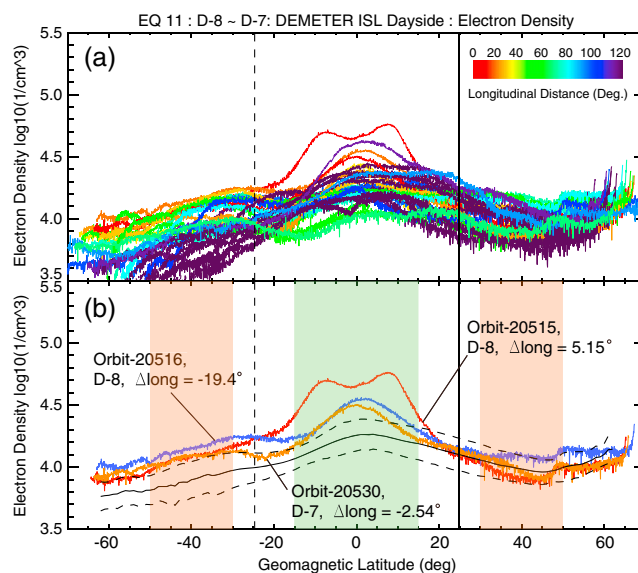


Figure 3. Latitudinal profiles of the ionospheric electron density (N_e) measured by the DEMETER ISL in the dayside from D-8 to D-7 (4–5 May 2008). The graphs present (a) the profiles of all orbits with varying longitudinal distances from the epicenter whose color varies according to the color bar shown on the graph and (b) the latitudinal profiles of orbits whose longitudinal distances were less than 20° from the epicenter. The solid and dashed lines represent the average and 1σ range of the orbit profiles. The green and orange boxes on the graph represent the latitudinal range used to define the equatorial electron density (15°S – 15°N) and the midlatitude electron density (30°N – 50°N).

The increased electron density in the geomagnetic equator region can be defined as an enhanced EIA (equatorial ionization anomaly) and can be quantified using an EIA strength index. In this study, the strength of the EIA is represented as the equatorial plasma density normalized using the midlatitude density [Ryu *et al.*, 2014a], which is similar to the data presented by Kil *et al.* [2008] where they normalized the equatorial plasma density using the longitudinal mean density. The normalized equatorial plasma density (NEPD) is defined as the ratio of the averaged N_e in the region whose geomagnetic latitude is within $\pm 15^\circ$ (green box in Figure 3b) with respect to the averaged midlatitude N_e (30°S – 50°S and 30°N – 50°N in the geomagnetic latitude; the orange boxes in Figure 3b). Because the NEPD is defined as a ratio of the equatorial electron density with respect to the midlatitude density, every orbit profile in the dayside has a characteristic NEPD value. The evolutions of the NEPD values near the epicenter (15° from the epicenter longitude) in the same season

of 2007–2009 are presented in Figure 4. The X axis in the graphs represents the days with respect to the Wenchuan earthquake. Because the earthquake occurred on the 133rd day of 2008, the days from the earthquake occurrence for 2007 and 2009 represent the days from the 133rd day of the year.

The average NEPD and 1σ range of the 6 year period of the DEMETER observations were indicated using the red lines and green bands in the graphs, respectively. The background behavior of NEPD can vary according to the solar cycle and orbit altitude change. The seasonal and longitudinal NEPD variations in the period of 2007–2009 coincide with the 6 year average within 5%, based on the analysis on the long-term behavior of the NEPD. In 2007, the NEPD were large in general that the statistical average reaching almost 4.0 in several orbits but not large as in 2008. In 2008, when the Wenchuan earthquake occurred, the NEPD were exceptionally large before the earthquake occurrence. The maximum NEPD were observed in Orbit-20515 on 4 May, which was 8 days before the earthquake. The NEPD value for 4 May was 4.8, which was higher than the $\sim 3\sigma$ range, as seen in Figure 4b. It is noteworthy that among the 27,236 orbits during the stable observation period of DEMETER (2005–2010), only 31 orbits had NEPD values that were 4.5 or larger, which corresponds to 0.1%, and 0.5% of all the orbits had 4.0 or larger values. It appears that the increase of the NEPD began before the peculiar increase on D-8. The NEPD exhibited an increasing trend from D-30 and some orbits in D-22 to D-15 had values larger than 4.0. However, the geomagnetic activity does not explain the exceptionally large NEPD on D-8 because there was a moderate geomagnetic storm on D-10 and the NEPD did not exhibit any coincident behavior. It is the same for the increments on D-22 to D-15 because a moderate geomagnetic storm with $Kp > 4.0$ started on D-19, as seen in Figure 2. After the peculiar increase on D-8, the NEPD gradually decreased within the 1σ range before the earthquake. Increments also existed after the earthquake (from D+10 to D+25), but it is not certain if the increases were related to seismic activity or other effects. In 2009, the NEPD values predominantly remained within the 1σ range as seen in Figure 4c. Some orbits had an increased NEPD value from the 120th day to the 150th day of the year (DOY), but the increments were significantly smaller compared with those in 2008.

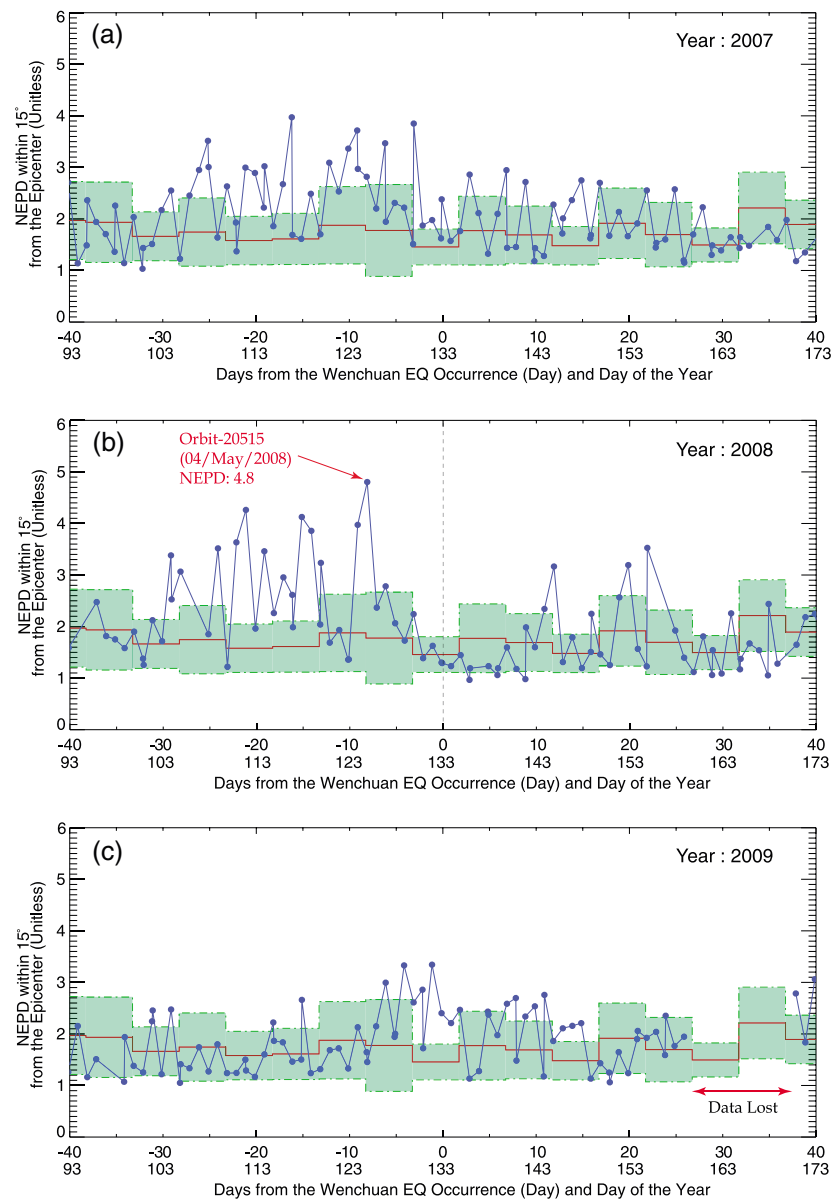


Figure 4. Temporal variations of the NEPD of the DEMETER satellite passes whose longitudes are within $\pm 15^\circ$ of the Wenchuan region from April to June (93rd DOY–173rd DOY) in the year (a) 2007, (b) 2008, and (c) 2009. The 6 year averages and variations are represented as red lines and green bands on the graphs.

Figure 5 presents the global seismic activity during the same periods. Each point in the graphs represents an earthquake magnitude, while the colors represent the longitudinal distance from that of the Wenchuan earthquake (103.365°E). The most apparent feature in the seismic activity in the spring time (93rd DOY–174th DOY) of 2007–2009 was the largest $M7.9$ Wenchuan earthquake and its aftershocks, which were depicted in red as seen in Figure 5b. While 2007 and 2008 were seismically active in the investigated period, the seismic activity in 2009 was particularly low and calm in the vicinity of the Wenchuan area. The Sumatra Arc seismic zone, which has a similar longitude range (90°E – 100°E) as the Wenchuan area was also calm in seismic activity in 2009. If the NEPD variations were solely related to the seismic activity, then the small NEPD in 2009 (Figure 4c) could be attributed to the absence of seismic activity (Figure 5c). The Wenchuan earthquake was characterized by an absence of foreshocks and extremely high aftershocks as seen in Figure 5b. This might have provided an ideal opportunity to identify the possible precursory seismo-ionospheric coupling with regard to the Wenchuan earthquake. While it is clear that the Wenchuan earthquake and its aftershocks were the main seismic activity on a global scale in 2008, as well as in the regional

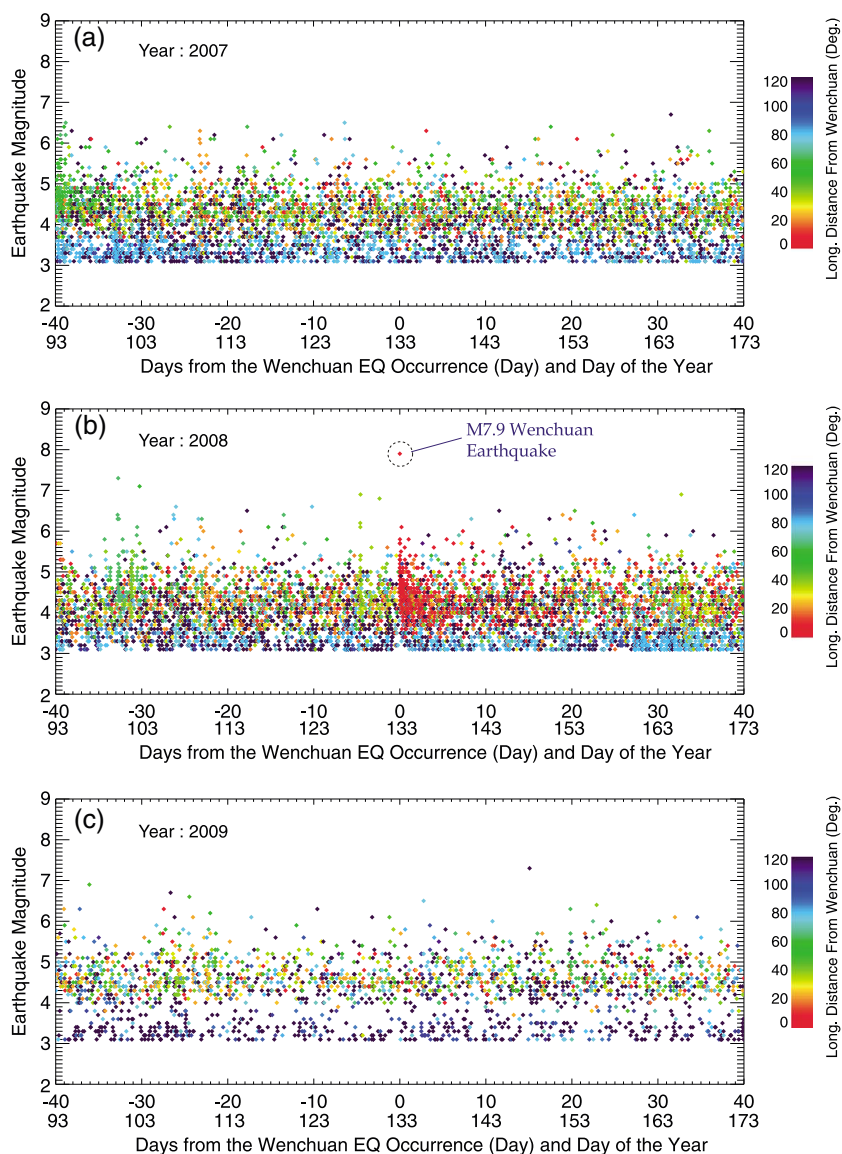


Figure 5. The seismic activity from April to June (93rd DOY to 173rd DOY) in the year (a) 2007, (b) 2008, and (c) 2009. The longitudinal distances from the Wenchuan earthquake are represented using varying colors as indicated by the color bar, while the y axis represents the earthquake magnitudes.

perspective, the distribution of earthquakes in 2007 (Figure 5a) was somewhat complicated. Near the longitudinal region of Wenchuan ($\sim 100^\circ\text{E}$), which was colored using orange and red, a series of earthquakes ($M \sim 6.0$) occurred on the 109th day of 2007. In addition, sporadic earthquakes with moderately large magnitudes ($4.0 < M < 6.0$) occurred in the period from the 115th day to the 140th day, which approximately coincides with the period when the NEPD were relatively large. The possibility that the enhanced EIA observed in 2007 also resulted from the seismo-ionospheric coupling cannot be discarded.

In order to determine whether the precursory EIA enhancements were only seasonal or global enhancements due to space weather or geomagnetic activity, or whether they were genuine seismo-ionospheric couplings related to the Wenchuan earthquake, the daily longitudinal variations during the studied period were plotted in Figure 6. The statistical averages and standard deviations of the NEPD during the DEMETER observation period (2005–2010) were presented together as red lines and green bands, respectively, in the plots. The values were derived for 5° intervals in the longitudinal direction and for 5 day intervals. Because DEMETER had a Sun-synchronous orbit, daily observations of 14–15 orbits generated longitudinal variations of the EIA intensity at the fixed local time. The black squares represent the NEPD values derived from

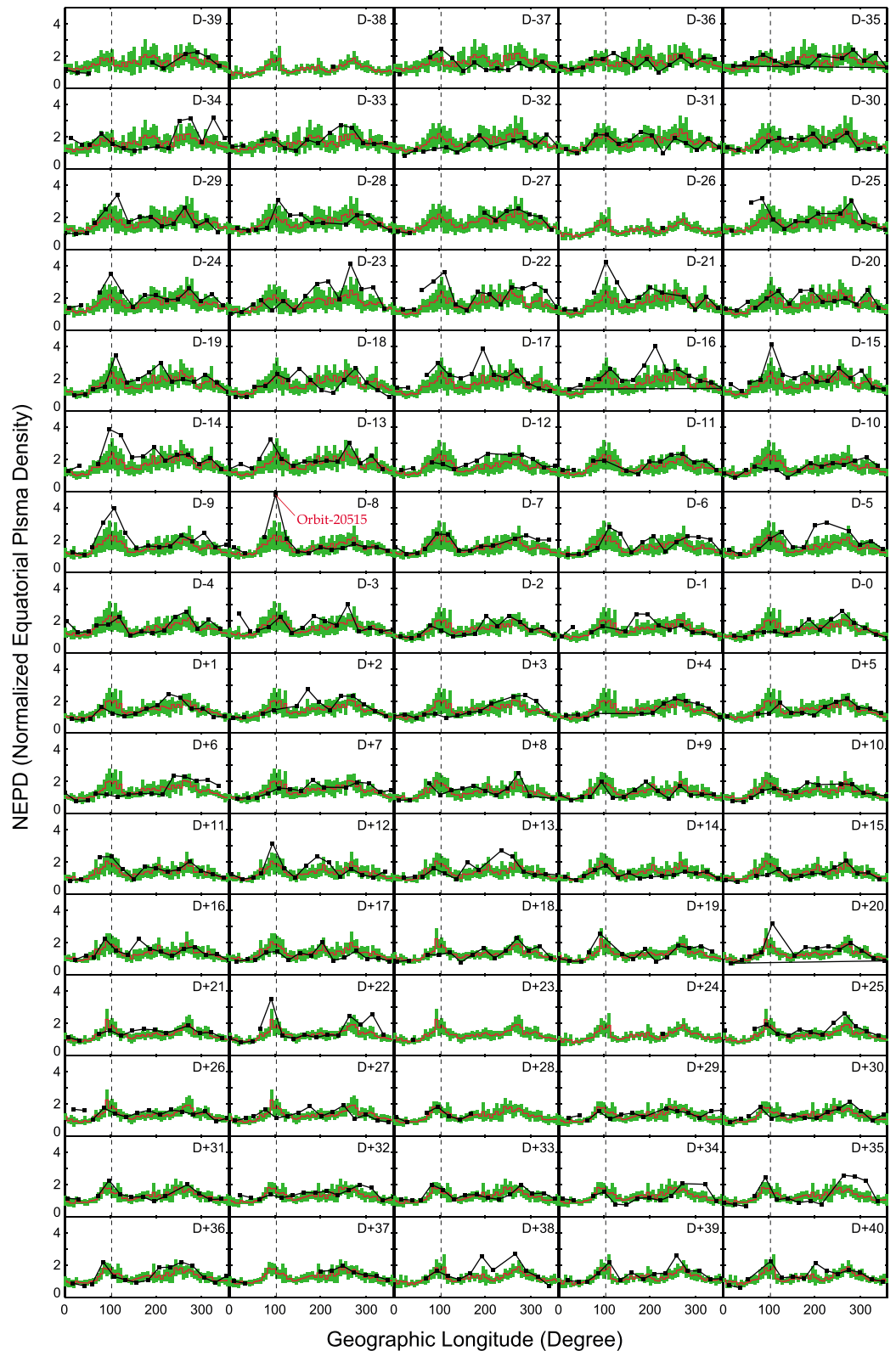


Figure 6. The daily variations of the longitudinal distribution of the NEPD from D-39 to D+40 with respect to the Wenchuan earthquake of 12 May 2008. The red lines and green bands represent the averages and deviations derived from DEMETER's stable observation in the period from 2005 to 2010.

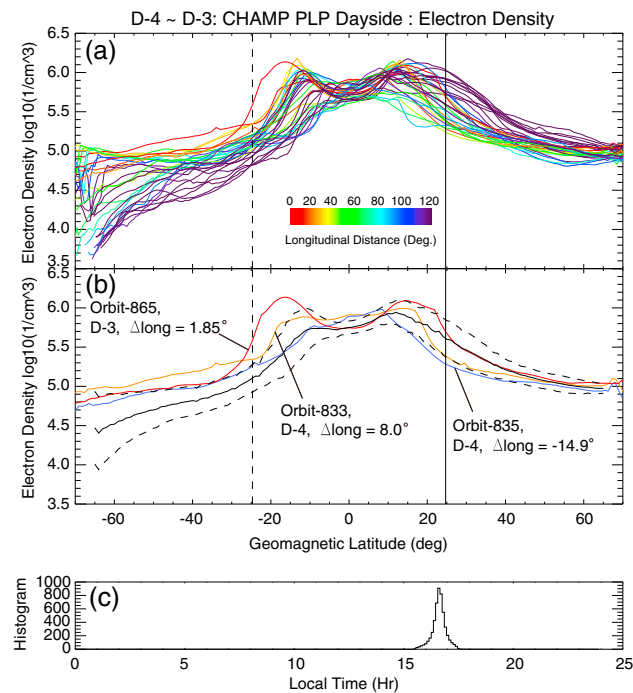


Figure 7. Latitudinal profiles of the ionospheric electron density (N_e) measured by CHAMP PLP in the dayside from D-4 to D-3 (8–9 May 2008). The graphs present (a) the profiles of all orbits with varying longitudinal distances from the epicenter whose color varies according to the color bar in the graph and (b) the latitudinal profiles of the orbits whose longitudinal distances are less than 20° from the epicenter. The solid and dashed lines represent the average and 1σ range of the orbit profiles. (c) This graph represents the local time distributions of the data observation points.

3.2. CHAMP and GPS TEC Observations

The possible correlations of the exceptional increases of the EIA strength measured by DEMETER with the seismic activities linked to the Wenchuan earthquake of 2008 were investigated. The longitudinal variations support the possibility in the sense of space as well as time, since the increases of the NEPD were limited to the region around the epicenter. It is not certain that the intensified EIA is a typical feature that can only be seen in the DEMETER local time (10:30). CHAMP was also operational during the same period with varying local times due to the precession. Around the time of the Wenchuan earthquake, the orbit plane of CHAMP was located in the local time between 16:00 and 17:00, which is after the daily EIA intensity is maximized. In addition to the local time, the altitude of CHAMP was significantly lower than that of DEMETER, which results in a difference in the N_e profile.

Some orbits that passed the epicenter were identified to have enhanced EIA features with increased crest geomagnetic latitudes. The most apparent enhancement was found in Orbit-865 on D-3 that passed 1.85° east of the epicenter, as seen in Figure 7. Figure 7a presents the latitudinal (geomagnetic) profile in the period from D-4 to D-3. The longitudinal distance from the epicenter was represented as varying colors. The N_e profiles of the orbits with longitudinal distances of less than 15° from the epicenter are presented separately in Figure 7b. The crest positions of Orbit-865 were most extended to the poleward directions and the peak electron densities at the crests were significantly larger than the longitudinal average and standard deviation ranges represented using solid and dashed black lines, respectively.

However, the time when the EIA observed by CHAMP was intensified did not coincide with that when the EIA was enhanced in the DEMETER observation. On days D-3 and D-4 when CHAMP showed the intensified EIA features, the DEMETER N_e profile did not show any peculiar behavior near the epicenter as shown in Figures 4 and 6. The most obvious differences of CHAMP and DEMETER which can explain the different behavior are the altitude and local time (see Figure 7c). This implies that the seismo-ionospheric coupling

the latitudinal profile of the electron density. The most conspicuous feature in the graphs is that the NEPD of Orbit-20515 on D-8 had the largest value during the studied period and its longitude coincided with that of the epicenter of the Wenchuan earthquake, which was represented as vertical lines in the graphs.

The longitudinal EIA enhancement along the epicenter of the Wenchuan earthquake began from \sim D-29, with a maximum intensity on D-8, and then diminished afterward. The limited longitudinal range of the EIA enhancement excluded the possibility that the intensified EIA was caused by space weather or geomagnetic activity that affected the global ionosphere in general, rather than a specific longitude. Enhancements in the EIA feature appeared in the same longitudinal region on D+20 and D+22, which were also shown in Figure 4b. They might be related to a series of large earthquakes on D+23 that appear as red dots in Figure 5b. The largest earthquake among the series of aftershocks is EQ-48, in Table 1, with $M6.1$ and a depth of 18.0 km.

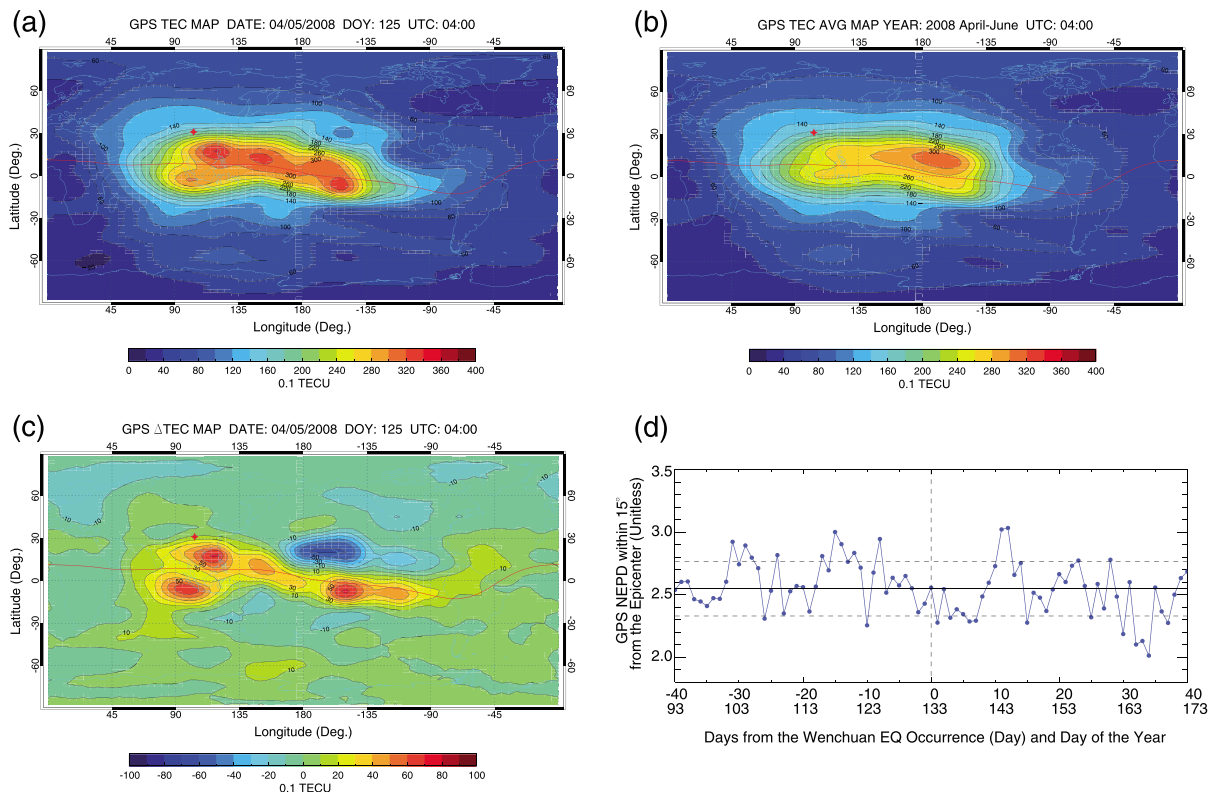


Figure 8. (a) GPS TEC map on 4 May 2008 (D-8) at 04:00 UTC, (b) averaged GPS TEC map of 04:00 UTC from April to June 2008, (c) Δ TEC map (a)-(b) that illustrates the deviation of the TEC from the seasonal average on May 4, and (d) the daily evolution of the NEPD derived using the GPS TEC in the longitude range $\pm 15^\circ$ from the epicenter at 04:00 UTC.

might be a complicated function of local time and altitude, as well as geometry of the electromagnetic phenomena involved in the process. It seems that the anomalous increase of the EIA features observed by DEMETER and CHAMP around the Wenchuan longitude show slowdown before the upcoming earthquake. It is noteworthy that the increase and slowdown profile of the fountain effect resembles that of the gradual variation of the electric field of the earth which is a transient anomaly of long duration (of the order of 1 month) before large earthquakes [Varotsos *et al.*, 2011].

A number of studies [Zhao *et al.*, 2008; Pulinets *et al.*, 2010; Klimenko *et al.*, 2011] have reported increased TEC prior to the Wenchuan earthquake derived from the GPS dual-frequency sounding method. Those studies have only focused on the ionospheric disturbances in May 2008, while this study has demonstrated that the intensified EIA derived from the electron density measured by DEMETER began from the middle of April and had its peak intensity on D-8 (4 May). In this study, the global maps of vertical TEC of the ionosphere provided by the IGS [Hernández-Pajares *et al.*, 2009] with 2 h intervals were used to verify whether the observed EIA enhancement also appeared in the global TEC map.

As noted above, the EIA intensity represented in the NEPD values had its maximum during the study period in Orbit-20515 on D-8. DEMETER passed the equator in a descending node at $\sim 03:20$ UTC, 4 May, in Orbit-20515. Accordingly, the IGS VTEC map of 04:00 UTC is the most adjacent to Orbit-20515 from the temporal perspective. The global TEC map at 04:00 UTC 4 May 2008 is presented in Figure 8a. The EIA feature in the dayside (90°E – 225°E) is clearly seen as increased TEC to 30 total electron content unit (TECU) (10^{16} m^{-2}) along the geomagnetic dip equator. The epicenter, which is marked with a red star in the map, is at $\sim 11:00$ LT and right before the daily EIA feature begins to emerge from the east. However, it is difficult to conclude that the TEC distribution is abnormal compared with the seasonal behavior based on the map alone.

The method of deriving the Δ TEC map as described by Klimenko *et al.* [2011] was used in the analyses of the TEC disturbances prior to the Wenchuan earthquake. Figures 8b and 8c represent the seasonal averages and Δ TEC map, respectively. The seasonal average map was derived through numerically averaging the

GPS maps obtained during the period from April to June 2008, which encompasses the earthquake occurrence. The Δ TEC map was derived through subtracting the seasonal average (Figure 8b) from the TEC map (Figure 8a) and it is presented in Figure 8c. It is apparent that the region with longitudes close to the epicenter had increased EIA features with TEC values larger than the seasonal average by 6–7 TECU. Positive and negative disturbances exist around 200°E in the middle of the Pacific Ocean; however, the reason for these disturbances is not clear and is beyond the scope of this study.

Analogous to the DEMETER electron density, the NEPD can be derived for the GPS TEC by normalizing the equatorial TEC with respect to the midlatitude TEC averaged in the longitude range $\pm 15^\circ$ from the epicenter. Figure 8d shows the daily evolution of the GPS NEPD. Though the evolution of the GPS NEPD is not exactly following the DEMETER (N_e) NEPD and the magnitudes of the peaks are not directly proportional to each other, the GPS NEPD shows clear increment whenever the DEMETER NEPD increases (e.g., D-29, D-14, D-8, and D+12). This could be because that the DEMETER NEPD is more sensitive to the plasma movement in the F_2 region while the GPS NEPD reflect the change of total electron contents. However, it can be said that the DEMETER NEPD evolution, which reflects the change in the higher altitude, could be complementarily confirmed by the GPS NEPD.

3.3. Nighttime Observations and Electric Field Measurements

The EIA enhancements in the dayside ionosphere related to the Wenchuan earthquake were investigated using the satellite data (DEMETER and CHAMP) and the GPS TEC maps. If the features are bound to the lithospheric phenomena (i.e., seismo-ionospheric coupling), there should also be anomalies in the nightside. *Kuo et al.* [2014] noted that the depletion region of electron density caused by the seismically generated zonal electric field could trigger an equatorial plasma bubble (EPB) in the low geomagnetic latitude region, but their assertion on the nighttime ionosphere around the seismic zone lacks observational evidence. *Burke et al.* [2004] noted that EPBs are prone to occur when the magnetic flux tubes are aligned with the dusk terminator. In addition, tropospheric gravity waves have also been identified as a source of EPB occurrences [*Hysell et al.*, 1990].

The nighttime ionosphere observed by DEMETER was investigated in order to identify possible seismo-ionospheric coupling. There were unclear signatures of EPB occurrences in this period. Even for the EPB occurrences, they were not likely to be spatially related to the seismic zone. As noted above, the EIA enhancement in the daytime ionosphere was maximized on D-8 (4 May) in Orbit-20515 that passed 5.15° east of the epicenter. Figure 9 presents the nighttime ionospheric conditions in the period from D-8 to D-7, which were measured by the IAP and ISL instruments installed on DEMETER. The period encompasses the successive night (Orbit-20522) of Orbit-20515 and the next night (Orbit-20536) when DEMETER passed near the epicenter. Figure 9a presents the latitudinal profiles of the O^+ density measured by the IAP according to the longitudinal distances from the epicenter. In general, the Northern Hemisphere has a higher O^+ density. An orbit close to the epicenter, which is indicated in red, has an atypical profile compared with the other orbits because the O^+ density from the geomagnetic equator to the Northern Hemisphere was significantly reduced. This atypical reduction of O^+ density in the Northern Hemisphere near the epicenter region can also be found in the periods of D-12 to D-11 and D-6 to D-3.

The closest two orbits whose longitudinal distances were less than 15° are presented separately in Figure 9b. The blue line indicates Orbit-20522 on D-8, which passed 12.6° west of the epicenter, and the red line represents Orbit-20536 on D-7, which passed 4.2° east of the epicenter. The orange and green dotted lines represent H^+ and He^+ ion densities along Orbit-20536, respectively. In Orbit-20536, which passed closest to the epicenter during the period, the O^+ density had an asymmetric peak at the epicenter geomagnetic latitude. With the increase of the O^+ density around the geomagnetic latitude of the epicenter as the center, the equatorward O^+ density was significantly reduced compared with the poleward O^+ density. This asymmetric density profile (dotted circles in Figures 9b and 9c) was also found in the N_e measured by the ISL, as seen in Figure 9c. The asymmetric electron density profile above the epicenter latitude consistent with the asymmetric O^+ density fluctuation implies that the atypical behavior was possibly caused by a plasma drift rather than a chemical interaction within the ionosphere. The anomalous behavior of the light ionospheric ions was reported before the M6.4 Iranian earthquake of June 1990 [*Boskova et al.*, 1994]. The discrepancy in the absolute values of N_e and ion densities is thought to be caused by the incomplete intercalibration of the instruments. *Zhang* [2014] pointed out that the relative variation in T_e and N_e measured by the ISL instrument ought to be credible, while the absolute values of the electron density and temperature may not be

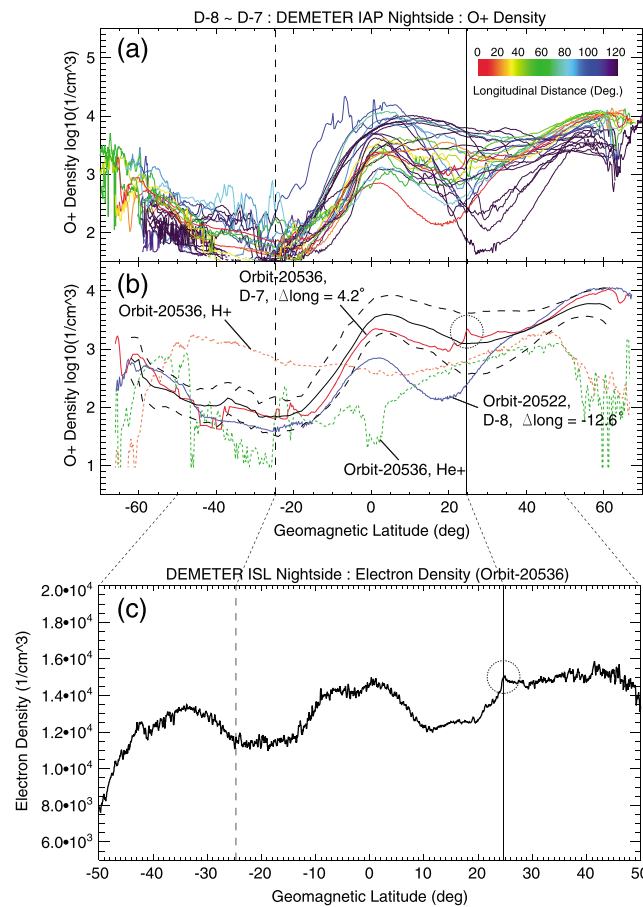


Figure 9. Latitudinal profiles of the O⁺ density measured by the DEMETER IAP in the nightside from D-8 to D-7 (4–5 May, 2008). The graphs present (a) the profiles of all orbits with varying longitudinal distances from the epicenter whose color varies according to the color bar and (b) the latitudinal profiles of the orbits whose longitudinal distances are less than 15° from the epicenter. The solid and dashed lines represent the average and 1σ range of the orbit profiles. The brown and green dashed lines represent H⁺ and He⁺ density profiles of Orbit-20536. (c) This graph presents the latitudinal profile of the electron density along Orbit-20536. The specific fluctuations in the O⁺ and electron density profiles are marked with dotted circles.

accurately determined. In addition, Wang *et al.* [2011] reported that the IAP grid transparency actually lower than the designated value, which can lead to lowered ion density.

Regardless of the latitude or altitude, the plasma motion was triggered by the electric field in general through an $\mathbf{E} \times \mathbf{B}$ drift [Kelley, 1989]. The ULF (DC–15 Hz) waveform measured by the ICE (Instrument Champ Electric) [Berthelier *et al.*, 2006a] on-board DEMETER was investigated in order to understand the density anomaly in the vicinity of the epicenter. Because the DEMETER spacecraft is three-axis stabilized, there can be a slowly varying bias electric field up to a few mV/m. Due to the relative stability of the electrode surface potential in time, small-scale electric field variations can be measured accurately [Piša *et al.*, 2011].

Figure 10 presents the ULF waveform measured in the two nightside orbits mentioned above. The dayside orbit data were contaminated by the photoelectron effect in the study period and were not considered in this study. The induced $\mathbf{v} \times \mathbf{B}$ components, which were caused by the motion of the satellite across the Earth's geomagnetic field, were eliminated from the original measurements. Therefore, the data processed from the velocity of the satellite and the value of geomagnetic field from the IGRF (International Geomagnetic Reference Field) model [Finlay *et al.*, 2010] were used to calculate the corresponding induced electric field.

Figures 10a and 10b present the E_x , E_y , and E_z components for Orbit-20522 and Orbit-20536, respectively. Because DEMETER had a polar orbit and ascends in the nightside, the +X direction represents the nadir (Earth direction), while –Z direction represents the velocity vector (quasi northward direction) and +Y direction is normal to the orbit (quasi eastward direction) in each graph. Orbit-20522 was characterized by the anomalous decrease of O⁺ density from the equator to the epicenter latitude, as depicted in Figure 9b. For the electric field, the eastward component (+ E_y) was intensified near the equator. Near the epicenter latitude, the E_z component (depicted by arrows in Figure 10a) exhibited an asymmetric disturbance. With the epicenter latitude as the center, the E_z was reduced in the south and intensified in the north. The latitudinal size of the disturbance was ~10° and the intensity of the perturbed electric field was about 2–3 mV/m. There are larger deviations of the electric field in the poleward directions which are attributable to the slowly varying bias electric field inevitable for three-axis stabilized satellite as mentioned earlier in this section. Considering that the northward electric field could trigger a westward $\mathbf{E} \times \mathbf{B}$ drift in the Northern Hemisphere and the DEMETER satellite local time was ~22:30 in the evening section when the ion density is lower in the east, the observed ion density profile is consistent with the electric field disturbances.

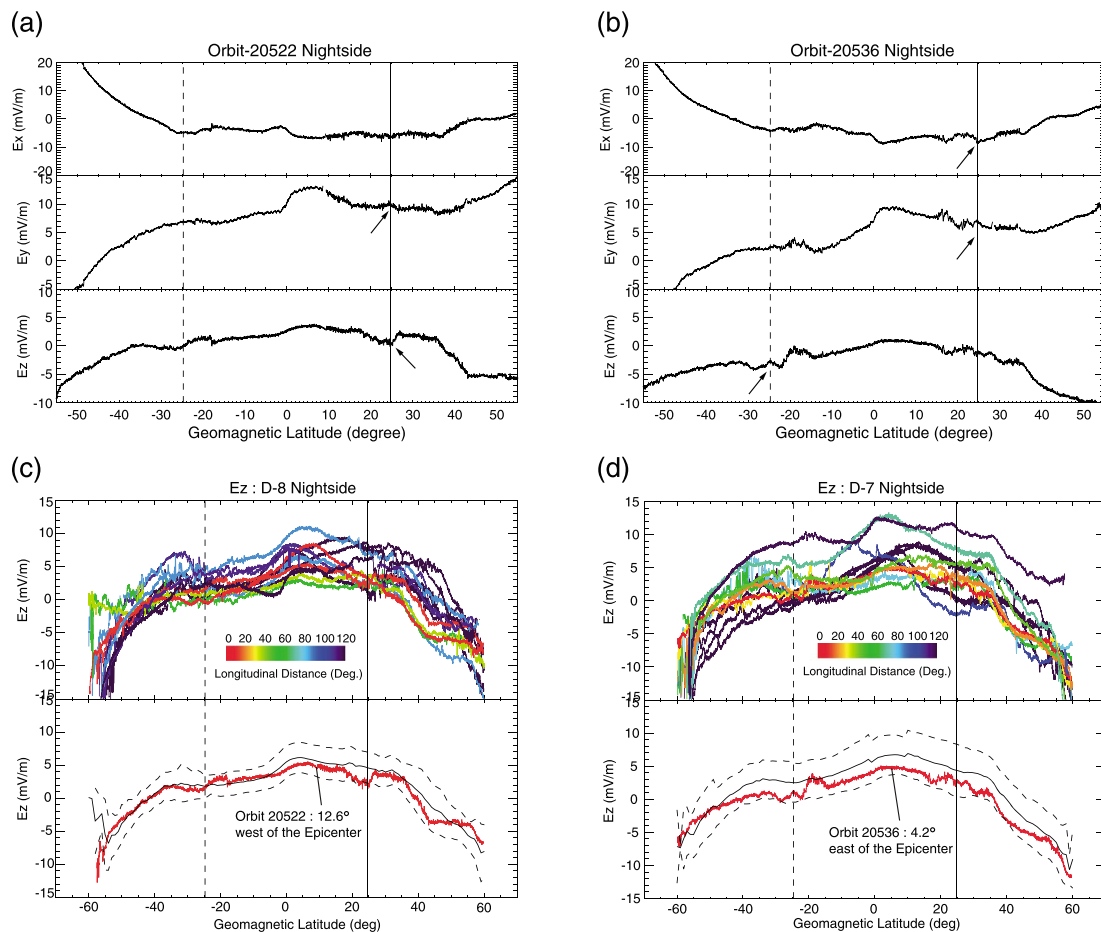


Figure 10. The electric field measured by the DEMETER ICE along (a) Orbit-20522 and (b) Orbit-20536. The E_x , E_y , and E_z components are indicated separately. The E_z profiles of all orbits in (c) D-8 and (d) D-7, with varying longitudinal distances from the epicenter whose color varies according to the color bar. The solid and dashed lines represent the average and 1σ range of the orbit profiles. The vertical solid and dashed lines represent the geomagnetic latitude of the epicenter and its conjugate latitude.

For Orbit-20536, the E_x , E_y , and E_z components commonly exhibited disturbances near the epicenter latitude. The E_z component exhibited a similar pattern in that the E_z was reduced south of the epicenter. The colored latitudinal profiles of D-8 and D-7 at different longitudes in the same manner as for density data are shown in Figure 10c and 10d. The absolute values of the electric field in Orbit-20522 (Figure 10c) and Orbit-20536 (Figure 10d) does not show clear deviation from the 1σ range. This suggests that the electric field fluctuations in these orbits does not show clear signatures of precursory or seismically excited fluctuation in the sense of the absolute value. Meanwhile, the latitudinal fluctuations within the orbits with magnitude $\sim 1\sigma$, whose location coincide with the epicenter or its geomagnetic conjugate, suggest that the electric field fluctuation could be involved in the density fluctuations and used as a supplementary physical quantity in studying seismo-ionospheric coupling or the earthquake precursors. In addition, the complete electric field configuration at the time of disturbance could not be determined, because the satellite observations were limited to in situ measurements. However, the electric field observations indicate that the disturbances in the ion density or electron density caused by the seismo-ionospheric coupling were the consequences of the complicated interactions of the plasma with the electromagnetic field configuration.

4. Discussion

Reductions in the atomic oxygen and molecular ion densities observed by the US satellite DE-2 around the M7.1 Chilean coast earthquake of October 1981 were reported as an EIA-like feature centered around the earthquake epicenter [Oyama *et al.*, 2011]. The ion density reduction was explained as a superposition of a quiet time eastward electric field and an electric field associated with the earthquake. Pulinets [2012]

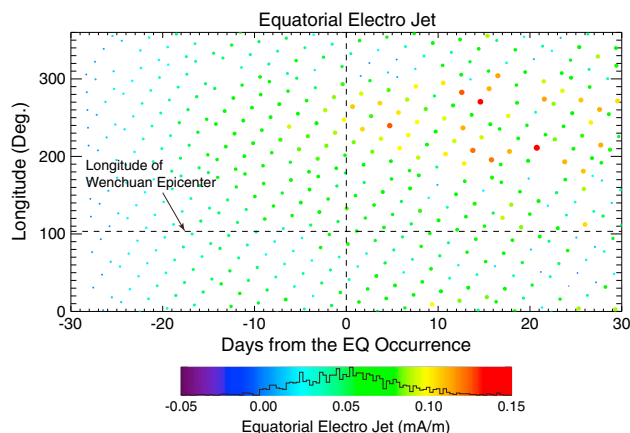


Figure 11. The equatorial electrojet (EEJ) derived from the CHAMP magnetometer measurement during the studied period (from 30 days before and to 30 days after the Wenchuan earthquake). Each colored circle represents the EEJ value for each orbit pass with the given equatorial crossing longitude in the dayside. The horizontal dashed line represents the longitude of the epicenter. The curve in the color bar is the normalized histogram of the EEJ values.

of August 2007 observed by the CHAMP and DEMETER satellites. It was explained that the change in the ionospheric potential over the seismic region accompanied a converging zonal electric field that triggered an upward (downward) plasma movement. They used the latitudinal electron density variations to demonstrate the seismo-ionospheric coupling. The two earthquakes were both located in the equatorial region, which naturally affects the equatorial ionosphere. In low latitudes, the ionosphere is dominated by electrodynamics through $\mathbf{E} \times \mathbf{B}$ drift. Hence, the enhancement of EIA before Wenchuan earthquake was definitely caused by an external enhanced electric field. On the other hand, it is possibly due to the process originating in the lower atmosphere, termed as “meteorological” by *Rishbeth and Mendillo* [2001]. In principle, electron density in F region can be affected by upward propagating atmospheric waves such as tides, planet waves, and atmospheric gravity waves, through modification of composition, temperature, and wind structure of the thermosphere. Simultaneously, E region electric field can also be affected through the dynamo mechanism [Forbes, 1996], leading to a high day-to-day variability and the asymmetric longitudinal structure in EIA. The statistical behavior of the longitudinal structure and its implication in the seismo-ionospheric anomaly was already studied by *Ryu et al.* [2014b].

This study demonstrated that the previously reported TEC increases were fragments of the gradually increased EIA intensity that began about a month before the main shock and had its maximum on D-8. The enhanced EIA features were observed correspondingly in the electron density data of the DEMETER satellite, CHAMP satellite, and the GPS TEC data. Considering that the geomagnetic latitude of the epicenter of the Wenchuan earthquake was 24.7°N , it could be suggested that the latitude of the seismic zone affecting the equatorial ionosphere through the seismo-ionospheric coupling processes be extended to $\sim 25^\circ$ in geomagnetic latitude.

Meanwhile, *Dabas et al.* [2006] and *Hajra et al.* [2009] demonstrated that equatorial electrojet (EEJ) strength is well correlated with EIA. To investigate whether the observed EIA enhancements were related with the EEJ variation, the EEJ values were derived from the CHAMP magnetometer [Maus et al., 2007] and shown in Figure 11. During the studied period (D-30 to D+30), the EEJ values did not show any increments along the epicenter longitude implying that the EIA enhancements observed along the epicenter longitude before the earthquake occurrence were not caused by the intensified EEJ. In May 2008, there observed increases of EEJ strength in the longitude range from 200° to 300° depicted as orange and red colors in Figure 11 and they are thought to be related with increased EIA features in the corresponding longitude range (See Figure 6).

In the nightside, systematic disturbances related to the seismic activity were not found as were found in the dayside ionosphere. Instead, peculiar latitudinal N_e and O^+ profiles were found in the orbits that passed close to the epicenter during the successive two nights after the EIA intensity was maximized (D-8) in the

reported that the longitudinal variation of f_oF_2 obtained with the IS-338 topside sounder was disturbed from the usual longitudinal structure 2 days prior to the $M7.3$ New Guinea earthquake of 16 July 1980. The distortion, i.e., the reduction of the f_oF_2 in the vicinity of the epicenter, was maintained until the day of the earthquake and then it disappeared. They explained that the longitudinal variations of the plasma density could result from the increased or decreased air conductivity through radon emanations in the epicenter region and followed by the decreased or increased ionospheric potential in the bottom of the F region ionosphere.

Recently, *Ryu et al.* [2014a] reported the EIA intensification prior to and after the $M8.7$ Sumatra earthquake of March 2005 and the $M8.0$ Pisco earthquake

dayside. The profiles were characterized by decreased O^+ density and N_e in the south of the epicenter and asymmetric increases in the north. The low-frequency (quasi DC) electric field measured by ICE in the nighttime passes also exhibited asymmetric disturbances with the epicenter latitude as the center. The directions of the electric field disturbances imply that the field was converging in the north-south direction. Walker *et al.* [2013] reported that increases in ULF activity existed in the vicinity of the epicenter of the Wenchuan earthquake. Considering that concurrent plasma density variations occurred in a large scale and the ULF frequency of the enhanced spectrum was less than a few Hz, the fluctuation in the ULF waveform could be considered as a DC variation rather than a wave phenomenon.

The density and electric field disturbances in the nightside could be understood using a combined view of Pulinets [2012] and Kuo *et al.* [2011]. They stated that the increased conductivity either by the radioactive radon gas emanated from the seismic zone [Ondoh, 2003] or by the positive hole charge carriers activated by the stressed rocks [Freund, 2010] could generate the current flow between the ground and the bottom of the ionosphere. While Pulinets [2012] postulated that the B field is horizontal so that only the zonal electric field had effect, Kuo *et al.* [2011] assumed a vertical B field at the bottom of the ionosphere when deriving the electric field configuration in order to obtain horizontally diverging or converging electric fields. Later, Kuo *et al.* [2014] modified their original model to be generalized to situations when the B field was oblique to the horizontal direction, which is applicable to the off-equatorial region. Unlike the original model [Kuo *et al.*, 2011], they assumed the finite conductivity (σ_{\parallel}) along the magnetic field in order that the current along the magnetic field line (J_{\parallel}) could be nonzero.

Figure 12 presents the electromagnetic configurations that can explain the observations introduced in this study. The electric field configurations were adopted from the perspectives of Pulinets [2012] and Kuo *et al.* [2011] for Figure 12a and of Kuo *et al.* [2014] for Figure 12b. At the midlatitude of the Northern Hemisphere, the B field direction is downward in the Northern Hemisphere as illustrated in the figure. The increased conductivity of the atmosphere over the seismic zone and the current flow cooperatively decrease (or increase) the ionospheric potential. Then, the electric field can be generated in radial directions in order to satisfy the continuity equation of the current density (\mathbf{J}) as $\nabla \cdot \mathbf{J} = 0$ as depicted in Figure 12a. The difference of Figure 12b is that the model [Kuo *et al.*, 2014] considered the finite conductivity along the magnetic field (σ_{\parallel}) while the other is based on the infinite conductivity. In the case of finite σ_{\parallel} , the electric field can be purely eastward or westward according to the current direction between the ground and the ionosphere as depicted in Figure 12b. The electric field perpendicular to the B field is transferred parallel along the geomagnetic field lines. Then, the plasma in the vicinity of the generated electric field is subject to the $\mathbf{E} \times \mathbf{B}$ drift motion as indicated by the arrows with various colors. If the ionosphere is observed in a satellite that travels from the south to the north in the nightside as in the DEMETER satellite situation, the E field along the satellite velocity would be disturbed asymmetrically with the seismic zone as the center, and the N_e and ion density are deviated accordingly (see Figure 12a); this is consistent with the observations by the DEMETER in the nightside of D-8 and D-7. Meanwhile, the eastward electric field which triggers the upward plasma drift and then the increase of the equatorial electron density could be the cause of the NEPD increase in the dayside that reached its maximum at D-8 as shown in Figure 6. It is not clear what determines the geometry of the electric field (purely eastward/westward or radial direction) and the following density variation. The possible causes of the variation are the stereoscopic configuration of the seismic activity, the ionospheric conductivity, the ionospheric potential, the local time, etc.

Rycroft *et al.* [2008] described the mechanism through which the air conductivity at the Earth's surface is modified and the consequent change for the ionospheric potential due to the apparition of electrical charges. Harrison *et al.* [2010, 2014] presented an application of this mechanism to earthquake processes. Pulinets and Ouzounov [2011] presented a Lithosphere-Atmosphere-Ionosphere Coupling model that explains the precursory phenomena of earthquakes. According to these, radon is continuously emanated from the Earth's crust, even without earthquakes, and the deviated radon emissions in the earthquake preparation period result in the ionospheric potential in the vicinity of the epicenter. However, debates remain about the mechanism through which the change of conductivity around the epicenter is created; thus, more observational and experimental evidence is required in order to resolve the controversy.

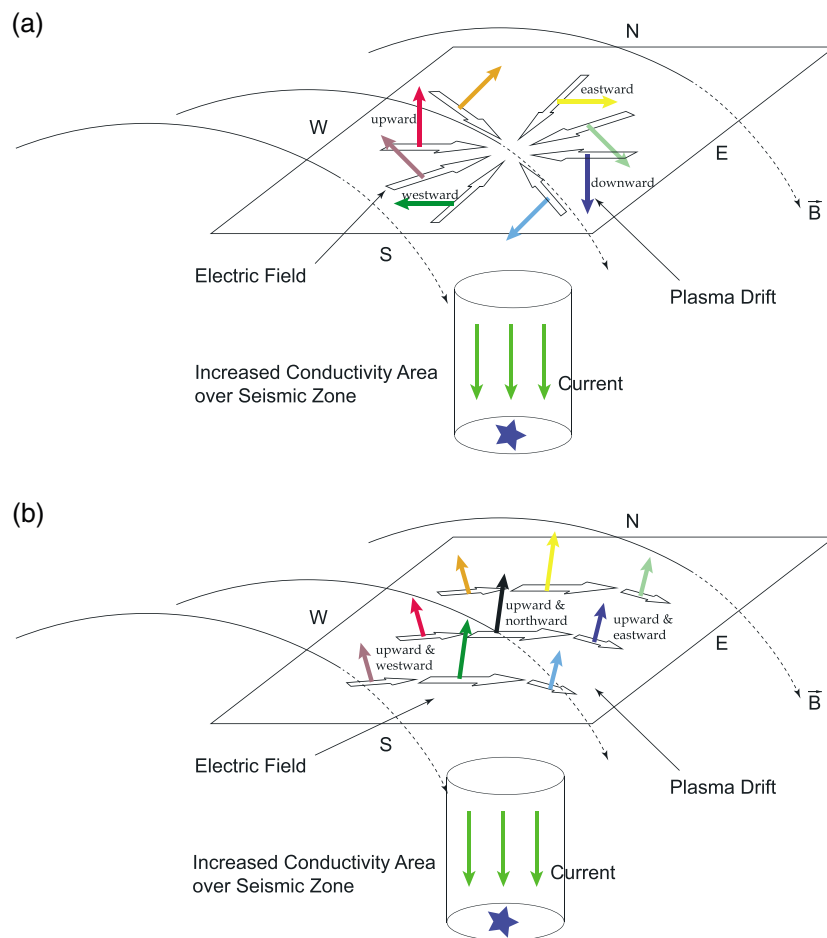


Figure 12. The electromagnetic and plasma drift configurations over the seismic zone that could explain the observed density and E field disturbances. The schematics were constructed from the perspectives of (a) the infinite ionospheric conductivity (σ_{\parallel}) model [Kuo et al., 2011; Pulinets, 2012] and of (b) the finite ionospheric conductivity model [Kuo et al., 2014].

5. Conclusions

The ionospheric disturbances related to the $M7.9$ Wenchuan earthquake of 12 May 2008 were investigated using the satellite measurements of DEMETER and CHAMP, in addition to the VTEC map derived from the global GPS stations. In the dayside ionosphere, the enhancements of the IIA intensity were observed before the earthquake occurrence both in the DEMETER and CHAMP N_e measurements, and these were confirmed with the GPS VTEC data. While the previous studies have typically reported on GPS TEC increases several days before the main shock, this study revealed that the increments were fragments of the gradually increased IIA strength near the epicenter longitude from approximately 1 month before and the IIA intensity expressed as the NEPD was exceptionally large on D-8 with weakening afterward. These anomalous features are strongly suspected as consequences of seismo-ionospheric coupling related to the Wenchuan earthquake. This indicates that the latitude of the epicenter, which can affect the equatorial ionosphere through the seismo-ionospheric coupling process, should be extended to $\sim 25^\circ$ in geomagnetic coordinates.

The disturbances in the electron and the O^+ density during the nightside and the concurrent perturbations in the electric field observed by the ICE instrument on-board DEMETER support that the ionospheric density disturbances were the result of $\mathbf{E} \times \mathbf{B}$ drifts caused by the ionospheric electric field generated over the epicenter. Finally, a detailed electromagnetic configuration, which is a combined view of the established explanations of the seismo-ionospheric coupling, was considered in order to explain the anomalous ionospheric behaviors observed by the satellites and ground GPS stations both in the dayside and nightside before the Wenchuan earthquake.

Acknowledgments

This work was supported by grant CATER2012-5060 from the Center for Atmospheric Science and Earthquake Research (CATER) in Korea. The authors are grateful to the engineers and scientists who were involved in the development, operation, and data processes of the DEMETER and CHAMP satellites. The authors also thank the International GNSS Service for providing the global maps of the vertical total electron content of the ionosphere. We also thank H. Kil at Johns Hopkins University Applied Physics Laboratory, J.J. Berthelier at LATMOS/ISSL, and J. P. Lebreton at LPC2E/CNRS for valuable comments on the behavior of the equatorial ionosphere and the data validity of the IAP and ISL. The DEMETER data used in this study were obtained via the CDDP data center (<http://cdpp2.cnes.fr/cdpp>), while the space weather data were obtained from the OMNI data center (<http://omniweb.gsfc.nasa.gov>). The GPS TEC data were downloaded from the CDDIS data center (<ftp://cddis.nasa.gov>) and the CHAMP data were obtained from the ISDC data center (<http://isdc.gfz-potsdam.de/>). In addition, the earthquake data were acquired from the USGS-NEIC data center (<http://earthquake.usgs.gov/regional/neic>).

Alan Rodger thanks Tong Xu and another reviewer for their assistance in evaluating this paper.

References

- Aleksandrin, S. Y., A. M. Galper, L. A. Grishantzeva, S. V. Koldashov, L. V. Maslennikov, A. M. Murashov, P. Picozza, V. Sgrigna, and S. A. Voronov (2003), High-energy charged particle bursts in the near-Earth space as earthquake precursors, *Ann. Geophys.*, *21*, 597–602.
- Berthelier, J. J., M. Godefroy, F. Leblanc, E. Seran, D. Peschard, P. Gilbert, and J. Artru (2006a), IAP, the thermal plasma analyzer on DEMETER, *Planet. Space Sci.*, *54*(5), 487–501, doi:10.1016/j.pss.2005.10.017.
- Berthelier, J. J., et al. (2006b), ICE, the electric field experiment on DEMETER, *Planet. Space Sci.*, *54*(5), 456–471, doi:10.1016/j.pss.2005.10.016.
- Boskova, J., J. Smilauer, F. Jiricek, and P. Triska (1993), Is the ion composition of the outer ionosphere related to seismic activity?, *J. Atmos. Terr. Phys.*, *55*, 1689–1695, doi:10.1016/0021-9169(93)90173-V.
- Boskova, J., J. Smilauer, P. Triska, and K. Kudela (1994), Anomalous behaviour of plasma parameters as observed by the intercosmos 24 satellite prior to the Iranian earthquake of 20 June 1990, *Stud. Geophys. Geod.*, *38*(2), 213–220, doi:10.1007/BF02295915.
- Burke, W. J., L. C. Gentile, C. Y. Huang, C. E. Valladares, and S. Y. Su (2004), Longitudinal variability of equatorial plasma bubbles observed by DMSP and ROCSAT-1, *J. Geophys. Res.*, *109*, A12301, doi:10.1029/2004JA010583.
- Chmyrev, V. M., N. Isaev, O. N. Serebryakova, V. M. Sorokin, and Y. P. Sobolev (1997), Small-scale plasma inhomogeneities and correlated ELF emissions in the ionosphere over an earthquake region, *J. Atmos. Terr. Phys.*, *59*(9), 967–974, doi:10.1016/S1364-6826(96)00110-1.
- Cussac, T., M.-A. Clair, P. Ultré-Guerard, F. Buisson, G. Lassalle-Balier, M. Ledu, C. Elisabelar, X. Passot, and N. Rey (2006), The DEMETER microsatellite and ground segment, *Planet. Space Sci.*, *54*, 413–427, doi:10.1016/j.pss.2005.10.013.
- Dabas, R., R. Das, V. Vohra, and C. Devasia (2006), Space weather impact on the equatorial and low latitude F-region ionosphere over India, *Ann. Geophys.*, *24*(1), 97–105.
- Finlay, C. C., et al. (2010), International Geomagnetic Reference Field: The eleventh generation, *Geophys. J. Int.*, *183*, 1216–1230, doi:10.1111/j.1365-246X.2010.04804.x.
- Forbes, J. M. (1996), Planetary waves in the thermosphere-ionosphere system, *Earth Planet. Space*, *48*, 91–98.
- Freund, F. (2010), Toward a unified solid state theory for pre-earthquake signals, *Acta Geophys.*, *58*(5), 719–766, doi:10.2478/s11600-009-0066-x.
- Fujiwara, H., M. Kamogawa, M. Ikeda, J. Y. Liu, H. Sakata, Y. I. Chen, H. Ofuruton, S. Muramatsu, Y. J. Chuo, and Y. H. Ohtsuki (2004), Atmospheric anomalies observed during earthquake occurrences, *Geophys. Res. Lett.*, *31*, L17110, doi:10.1029/2004GL019865.
- Gokhberg, M. B., I. L. Gufeld, A. A. Rozhnoy, V. F. Marenko, V. S. Yampolsky, and E. A. Ponomarev (1989), Study of seismic influence on the ionosphere by super long-wave probing of the Earth-ionosphere waveguide, *Phys. Earth Planet. Int.*, *57*, 64–67.
- Gutenberg, B., and C. F. Richter (1956), Magnitude and energy of earthquakes, *Annali di Geofisica*, *9*, 1–15.
- Hajra, R., S. Chakraborty, and A. Paul (2009), Electrodynamic control of the ambient ionization near the equatorial anomaly crest in the Indian zone during counter electrojet days, *Radio Sci.*, *44*, RS3009, doi:10.1029/2008RS003904.
- Harrison, R. G., K. L. Aplin, and M. J. Rycroft (2010), Atmospheric electricity coupling between earthquake regions and the ionosphere, *J. Atmos. Sol. Terr. Phys.*, *72*, 376–381, doi:10.1016/j.jastp.2009.12.004.
- Harrison, R. G., K. L. Aplin, and M. J. Rycroft (2014), Brief Communication: Earthquake-cloud coupling through the global atmospheric electric circuit, *Nat. Hazards Earth Syst. Sci.*, *14*, 773–777, doi:10.5194/nhess-14-773-2014.
- Hayakawa, M., O. A. Molchanov, T. Kodama, V. V. Afonin, and O. A. Akentieva (2000), Plasma density variations observed on a satellite possibly related to seismicity, *Adv. Space Res.*, *28*, 1277–1280, doi:10.1016/S0273-1177(99)01224-7.
- Hernández-Pajares, M., J. M. Juan, J. Sanz, R. Orus, A. Garcia-Rigo, J. Feltens, A. Komjathy, S. C. Schaer, and A. Krankowski (2009), The IGS VTEC maps: A reliable source of ionospheric information since 1998, *J. Geod.*, *83*, 263–275, doi:10.1007/s00190-008-0266-1.
- Hysell, D. L., M. C. Kelley, W. E. Swartz, and R. F. Woodman (1990), Seeding and layering of equatorial spread F by gravity waves, *J. Geophys. Res.*, *95*, 17,253–17,260, doi:10.1029/JA095iA10p17253.
- Kelley, M. C. (1989), *The Earth's Ionosphere—Plasma Physics and Electrodynamics*, 1st ed., 38 pp., Acad. Press, New York.
- Kil, H., E. R. Tallat, S.-J. Oh, L. J. Paxton, S. L. England, and S.-Y. Su (2008), Wave structure of the plasma density and vertical EXB drift in low-latitude F region, *J. Geophys. Res.*, *113*, A09312, doi:10.1029/2008JA013106.
- Klimenko, M. V., V. V. Klimenko, I. E. Zakharenkova, S. A. Pulnina, B. Zhao, and M. N. Tsidilina (2011), Formation mechanism of great positive TEC disturbances prior to Wenchuan earthquake on May 12, 2008, *Adv. Space Res.*, *48*, 488–499, doi:10.1016/j.asr.2011.03.040.
- Kuo, C. L., J. D. Huba, G. Joyce, and L. C. Lee (2011), Ionosphere plasma bubbles and density variations induced by pre-earthquake rock currents and associated surface charges, *J. Geophys. Res.*, *116*, A10317, doi:10.1029/2011JA016628.
- Kuo, C. L., L. C. Lee, and J. D. Huba (2014), An improved coupling model for the lithosphere-atmosphere-ionosphere system, *J. Geophys. Res. Space Physics*, *119*, 3189–3205, doi:10.1002/2013JA019392.
- Larkina, V. I., V. V. Migulin, O. A. Molchanov, I. P. Kharkov, A. S. Inchin, and V. B. Schvetcova (1989), Some statistical results on very low frequency radiowave emissions in the upper ionosphere over earthquake zones, *Phys. Earth Planet. Int.*, *57*, 100–109.
- Lebreton, J.-P., et al. (2006), The ISL Langmuir probe experiment processing onboard DEMETER: Scientific objectives, description and first results, *Planet. Space Sci.*, *54*(5), 472–486, doi:10.1016/j.pss.2005.10.017.
- Li, M., and M. Parrot (2013), Statistical analysis of an ionospheric parameter as a base for earthquake prediction, *J. Geophys. Res. Space Physics*, *118*, 3731–3739, doi:10.1002/jgra.50313.
- Liu, J. Y., Y. I. Chen, Y. J. Chuo, and C. S. Chen (2006), A statistical investigation of preearthquake ionospheric anomaly, *J. Geophys. Res.*, *111*, A05304, doi:10.1029/2005JA011333.
- Lühr, H., J. Park, P. Ritter, and H. Liu (2012), In-situ CHAMP observation of ionosphere-thermosphere coupling, *Space Sci. Rev.*, *168*, 237–260, doi:10.1007/s11214-011-9798-4.
- Maus, S., P. Alken, and H. Lühr (2007), Electric fields and zonal winds in the equatorial ionosphere inferred from CHAMP satellite magnetic measurements, *Geophys. Res. Lett.*, *34*, L23102, doi:10.1029/2007GL030859.
- McNamara, L. F., D. L. Cooke, C. E. Valladares, and B. W. Reinisch (2007), Comparison of CHAMP and Digisonde plasma frequencies at Jicamarca, Peru, *Radio Sci.*, *42*, RS2005, doi:10.1029/2006RS003491.
- Namgaladze, A. A., M. V. Klimenko, V. V. Klimenko, and I. E. Zakharenkova (2009), Physical mechanism and mathematical modeling of earthquake ionospheric precursors registered in total electron content, *Geomagn. Aeron.*, *49*(2), 252–262, doi:10.1134/S0016793209020169.
- Ondoh, T. (2003), Anomalous sporadic-E layers observed before M7.2 Hyogo-ken Nanbu earthquake; Terrestrial gas emanation model, *Adv. Polar Upper Atmos. Res.*, *17*, 96–108.
- Oyama, K.-I., Y. Kakinami, J. Y. Liu, M. Kamogawa, and T. Kodama (2008), Reduction of electron temperature in low-latitude ionosphere at 600 km before and after large earthquakes, *J. Geophys. Res.*, *113*, A11317, doi:10.1029/2008JA013367.
- Oyama, K.-I., Y. Kakinami, J. Y. Liu, M. A. Abdu, and C. Z. Cheng (2011), Latitudinal distribution of anomalous ion density as a precursor of a large earthquake, *J. Geophys. Res.*, *116*, A0431, doi:10.1029/2010JA015948.

- Parrot, M. (2002), The micro-satellite DEMETER, *J. Geod.*, *33*, 535–541, doi:10.1016/S0264-3707(02)00014-5.
- Píša, D., O. Santolík, and M. Parrot (2011), ULF waveform fluctuations above seismic active regions observed by the DEMETER satellite, in *WDS'11 Proceedings of Contributed Papers: Part II—Physics of Plasmas and Ionized Media*, edited by J. Safrankova and J. Pavlu, pp. 73–78, Matfyz press, Prague.
- Pulinets, S. (2012), Low-latitude atmosphere-ionosphere effects initiated by strong earthquakes preparation process, *Int. J. Geophys.*, *2012*, 131842, doi:10.1155/2012/131842.
- Pulinets, S., and D. Ouzounov (2011), Lithosphere-Atmosphere-Ionosphere Coupling (LAIC) model—An unified concept for earthquake precursors validation, *J. Asian Earth Sci.*, *41*, 371–382, doi:10.1016/j.jseas.2010.03.005.
- Pulinets, S. A., V. G. Bondur, M. N. Tsivilina, and M. V. Gaponova (2010), Verification of the concept of seismoionospheric relations under quiet heliogeomagnetic conditions, using the Wenchuan (China) earthquake of May 12, 2008, as an example, *Geomagn. Aeron.*, *50*(2), 231–242, doi:10.1134/S0016793210020118.
- Rishbeth, H., and M. Mendillo (2001), Patterns of F2-layer variability, *J. Atmos. Sol. Terr. Phys.*, *63*(15), 1661–1680, doi:10.1016/S1364-6826(01)00036-0.
- Rycroft, M. J., R. G. Harrison, K. A. Nicoll, and E. A. Mareev (2008), An overview of Earth's global electric circuit and atmospheric conductivity, *Space Sci. Rev.*, *137*, 83–105, doi:10.1007/s11214-008-9368-6.
- Ryu, K., E. Lee, J. S. Chae, M. Parrot, and K. I. Oyama (2014a), Multisatellite observations of an intensified equatorial ionization anomaly in relation to the northern Sumatra earthquake of March 2005, *J. Geophys. Res. Space Physics*, *119*, 4767–4785, doi:10.1002/2013JA019685.
- Ryu, K., E. Lee, J. S. Chae, M. Parrot, and S. Pulinets (2014b), Seismo-ionospheric coupling appearing as equatorial electron density enhancements observed via DEMETER electron density measurements, *J. Geophys. Res. Space Physics*, *119*, 8524–8542, doi:10.1002/2014JA020284.
- Sorokin, V. M., and V. M. Chmyrev (2002), Electrodynamic model of ionospheric precursors of earthquakes and certain types of disasters, *Geomagn. Aeron.*, *42*(6), 781–792.
- Tronin, A. A. (1996), Satellite thermal survey—A new tool for the study of seismoactive regions, *Int. J. Remote Sens.*, *17*, 1439–1455, doi:10.1080/01431169608948716.
- Tsurutani, B. T., and W. D. Gonzalez (1987), The cause of high-intensity long-duration continuous AE activity (HILDCAA): Interplanetary Alfvén wave train, *Planet. Space Sci.*, *35*, 405–412, doi:10.1016/0032-0633(87)90097-3.
- Varotsos, P., N. V. Sarlis, and E. S. Skordas (2011), *Natural Time Analysis: The New View of Time: Precursory Seismic Electric Signals, Earthquakes and other Complex Time Series*, pp. 13–15, Springer, Heidelberg, Berlin.
- Walker, S. N., V. Kadiramanathan, and O. A. Pokhotelov (2013), Changes in the ultra-low frequency wave field during the precursor phase to the Sichuan earthquake: DEMETER observations, *Ann. Geophys.*, *31*(9), 1597–1603, doi:10.5194/angeo-31-1597-2013.
- Wang, X., J. J. Berthelier, T. Onishi, S. Zhang, P. J. Erickson, J. P. Lebreton, M. Loiselet, and D. Lagoutte (2011), A comparison between DEMETER and the Millstone Hill ISR observations in a period of low solar activity, in *The 2nd International DEMETER Workshop*, Paris.
- Zhang, X. (2014), Electron density comparison between IRI 2007 and DEMETER satellite data in solar minimum year, *Terr. Atmos. Ocean. Sci.*, *25*(4), 559–571, doi:10.3319/TAO.2014.02.24.01(AA).
- Zhang, X., Z. Zeren, M. Parrot, R. Battiston, J. Qian, and X. Shen (2011), ULF/ELF ionospheric electric field and plasma perturbations related to Chile earthquakes, *Adv. Space Res.*, *47*(6), 991–1000, doi:10.1016/j.asr.2010.11.001.
- Zhao, B., M. Wang, T. Yu, W. Wan, J. Lei, L. Liu, and B. Ning (2008), Is an unusual large enhancement of ionospheric electron density linked with the 2008 great Wenchuan earthquake, *J. Geophys. Res.*, *113*, A11304, doi:10.1029/2008JA013613.